Improved Thermodynamic Descriptions of Carbides in Ni-Based Superalloys

RICHARD BUERSTMAYR,[1] BERND SCHULZ [id],[1,4] ERWIN POVODEN-KARADENIZ,[2] ERNST KOZESCHNIK,[2] MICHAEL LISON-PICK,[3] and SOPHIE PRIMIG [id] [1,5]

1.—School of Materials Science & Engineering, UNSW Sydney, Sydney, NSW 2052, Australia. 2.—Institute of Materials Science and Technology, TU Wien, 1060 Vienna, Austria. 3.—Western Australian Specialty Alloys, Perth, WA 6155, Australia. 4.—e-mail: b.schulz@unsw.edu.au. 5.—e-mail: s.primig@unsw.edu.au

The Ni-based superalloy René 41 has sparked recent interest for applications in next-generation aircraft engines due to its high-temperature strength that is superior to all similar grades. These desirable properties are achieved by careful control of the microstructure evolution during thermomechanical processing, and this is commonly informed by simulations. In particular, the grain boundary carbides M_6C and $M_{23}C_6$ play an essential role in controlling the grain size and strength of the final product. Therefore, a solid understanding of the thermodynamic stability and thermokinetic evolution of these carbides is essential. However, thermokinetic simulations using existing thermodynamic databases have been demonstrated to have discrepancies between thermodynamic stabilities and experimental observations. Here, we collected a new experimental time–temperature–precipitation diagram. In conjunction with improved crystallographic descriptions, these experimental results are used to modify a CALPHAD database for M_6C and $M_{23}C_6$. The modified database correctly identifies temperature regions with rapid carbide precipitation kinetics. Further, kinetic simulations and strengthening models successfully predict the hardness increase due to γ' precipitation. The modified database has been applied to Udimet 700, Waspaloy, and Haynes 282, demonstrating improved results. These updates will facilitate more accurate simulations of the microstructure evolution during thermomechanical processing of advanced Ni-based superalloys for aerospace and other applications.

INTRODUCTION

Cast and wrought γ'-strengthened Ni-based superalloys are established materials for applications where high dynamic loads, corrosive environments, and high temperatures intersect.[1] These properties are achieved by solid-solution and precipitation-strengthening of coherent γ' precipitates. Further, the addition of Cr provides the required corrosion resistance. Minor elements, such as B and C, are used to modify grain boundary properties in superalloys, either by segregation or by the formation of grain boundary precipitates.[2] René 41 is a Ni-based superalloy that is characterized by its exceptionally high strength and good fatigue properties when compared to similar alloys in the same class, such as Waspaloy and Haynes 282.[3,4] This has led to a renewed interest in René 41 as a candidate material for use in future generations of more fuel-efficient aircraft engines. However, this alloy exhibits complex precipitation kinetics, which makes control of the microstructural evolution and mechanical properties during thermo-mechanical processing challenging.[5–8] Generally, desirable properties are achieved by careful control of the microstructure evolution during thermomechanical processing of Ni-based superalloys, which is commonly supported by simulations.

Thermodynamic and thermokinetic modeling approaches are applied to evaluate the mechanical, microstructural, and physical properties of superalloys. This is useful in the selection of appropriate thermomechanical processing routes and heat treatments, as well as in the development of new and chemical finetuning of existing alloys.[9,10] The accuracy of such models strongly depends on the quality of their thermodynamic databases, which are used to evaluate the stabilities, compositions, and precipitation driving forces of the various phases present in an alloy system.[11,12] In the case of the superalloy René 41, a previous study by some of the current authors[13] revealed discrepancies in the phase stabilities between experimental observations and thermodynamic simulations, with respect to the phase stabilities and compositions of the M_6C and $M_{23}C_6$ carbides in particular. We showed that the currently available MCNI1 database for the simulation package MatCalc underestimates the M_6C and $M_{23}C_6$ solvus temperatures by 100–150 °C and 150–200 °C, respectively. Further, thermodynamic databases often rely on simplifications of phase descriptions. For example, in databases for Ni-based superalloys used in the software packages MatCalc and ThermoCalc, the descriptions of the M_6C and $M_{23}C_6$ carbides include sublattice descriptions that do not reflect their physical reality.[14–16] Although these simplifications in the thermodynamic descriptions reduce the computational expense of simulations, it sacrifices descriptive power and physical accuracy. Hence, modifications of these simplified phase descriptions of the M_6C and $M_{23}C_6$ carbides will improve their simulated phase stabilities and elemental compositions.

However, improvements in thermodynamic descriptions require empirically tested data. Some long-term stability data of precipitate phases in René 41 (up to 5000 h of thermal exposure times) have been published, but no systematic time–temperature–precipitation (TTP) data are publicly available to date.[8,17,18] Therefore, an experimental TTP diagram is developed in the present study. This will close the gap for shorter heat-treatment times (0.1–10 h) compared to already existing long-term heat-treatment studies. These insights, along with results from our previous study,[13] will provide a solid base for the advancement of thermodynamic descriptions of the relevant M_6C and $M_{23}C_6$ carbides, which is the aim of this study.

A first revision in thermodynamic description is applied to more accurately describe the crystal structure of these precipitates. In the second step, the thermodynamic parameters are fine-tuned to yield better results with respect to the stability and chemical composition. The adapted and original databases are then compared in kinetic simulations, evaluating grain boundary carbides M_6C and $M_{23}C_6$. The focus of these evaluations is phase stability and qualitative precipitation kinetics. Additionally, simulation results of γ' precipitation kinetics are presented. These results are evaluated based on the simulated strength increase and compared to experimental hardness tests. After optimization of the database for René 41, it was tested on alloys with similar constituent elements: Udimet 700, Waspaloy, and Haynes 282. This will explore possibilities and limitations in simulating M_6C and $M_{23}C_6$ carbides in other alloys. The latest version of the modified MCNI2b database is openly available under the name 'mc_ni_L.tdb' on https://www.matcalc.at/[19] and archived in Mendeley Data.[20]

In particular, these carbides are of interest due to their ability to provide grain boundary pinning during hot working, but also their ability to avoid deterioration of mechanical properties via the formation of embrittling grain boundary films.[8,21] As such, improving the predictive power of thermodynamic simulations can give insights into more appropriate hot-working and heat-treatment ranges for Ni-based superalloys.

EXPERIMENTAL AND SIMULATION APPROACH

Material and Heat Treatments

The material was provided by Western Australian Specialty Alloys (WASA) in the form of a disk cut from a billet after ingot-to-billet conversion, with a thickness of approximately 2.5 cm and a radius of approximately 30 cm. The billet was homogenized and mill-annealed by WASA. The chemical composition is shown in Table I. Samples were taken from a radial position of approximately 15 cm from the center of the billet. All the samples underwent an initial annealing step at 1200 °C for 30 min in an Ar atmosphere followed by water quenching, as depicted in Fig. 1a. The furnace used for these heat treatments was a Labec HTHTF50/16 tube furnace, and the temperature was controlled using a type K thermocouple. The solution annealed samples were then further sectioned into cubes with a geometry of approximately $1 \times 1 \times 1\ cm^3$. These cubes then underwent individual heat treatments at temperatures between 1150 °C and 600 °C in 50 °C intervals for time periods of 0.1, 1, and 10 h. All the cubes were inserted into the preheated furnace, isothermally annealed, and water-quenched to minimize changes of the microstructure during cooling.

After heat treatments, all the cubes were hot-mounted and metallographic preparation was conducted following standard grinding and polishing procedures, with a surface finish using a 0.04-μm colloidal silica suspension. The metallographic samples were then unmounted and attached to Al-sample holders to achieve better electrical conductivity for electron microscopy.

Experimental Time–Temperature–Precipitation and Hardness Evaluation

Scanning electron microscopy (SEM) micrographs and energy dispersive X-ray spectroscopy (EDS) line

Table I. The chemical composition of René 41 used in this study

	Ni	Cr[a]	Co[a]	Mo[a]	Ti[a]	Al[a]	Fe[a]	C[b]	B[a]	N[a]
at. %	Bal.	20.59	10.79	5.75	3.8	3.29	1.31	0.276	0.033	0.015
wt. %	Bal.	18.51	11	9.55	3.15	1.54	1.27	0.057	0.006	0.004

[a]Determined by X-ray fluorescence spectroscopy [b] Determined by low-element combustion oxidation
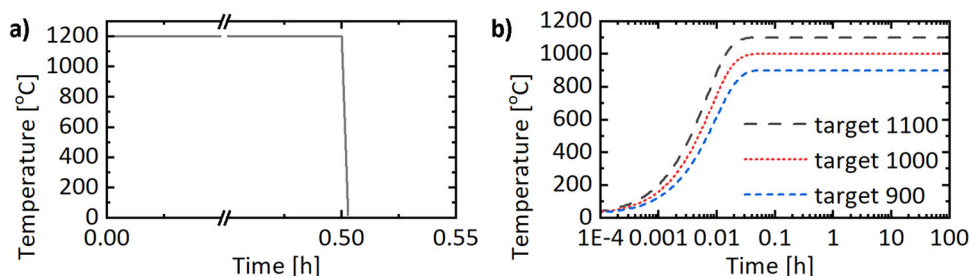

Fig. 1. (a) Initial solution-annealing profile at 1200 °C followed by rapid cooling (water quenching). (b) Numerical approximation of the time–temperature profiles during the heat treatments as used in the MatCalc simulations.

scans were collected on a Carl Zeiss AURIGA® CrossBeam® SEM. Unless otherwise specified, the micrographs presented here were collected using an electron backscattered detector at an acceleration voltage of 15 kV and a working distance of 7 mm. EDS was carried out with an acceleration voltage of 20 kV as an initial method to identify various carbides.

The phase fraction and precipitate size analysis of γ' precipitates within the matrix was determined based on SEM micrographs using a thresholding function in ImageJ (v.1.53f51).[22]

The analyses of grain boundary microstructures to determine the phase fraction of carbides were also carried out using ImageJ. Prior to the analyses, the matrix was manually cropped out of each image, leaving only the grain boundaries for further evaluation. Afterwards, selected precipitates at the grain boundaries were used to train the automated Weka segmentation plugin, generating a classifier function, which was then used on multiple grain boundaries to evaluate the various grain-boundary precipitates.[23] Prior to the evaluation of the precipitate size, a watershed function was applied. This function helps to more accurately evaluate adjacent precipitates that may wrongly be identified as the same precipitate. The precipitate diameters and respective standard deviations reported here were volume-weighted. This method was successfully applied to grain boundary precipitates at temperatures ranging from 1100 to 900 °C. At lower temperatures, the grain boundary precipitates were < 50 nm in diameter and deemed too small for accurate image analysis. Multiple grain boundary segments were analyzed, ensuring the results

are representative of the microstructure. An electron backscatter diffraction (EBSD; JEOL 7001 SEM) map was used to determine the grain boundary length density, i.e., the grain boundary length per unit area. This EBSD map has been published elsewhere (see Fig. 2c in Ref. [24]). Using this grain boundary length density of 64.5 cm^{-1}, the total phase fraction of grain boundary precipitates was estimated based on their occupancy at the grain boundaries.

Vickers hardness values were measured using a Struers Duramin 40 hardness tester with a load of 5 kg. To increase the reliability of the data presented here, each reported value is an average of 10 measurements. Based on the hardness test results, an empirical value of the yield strength was calculated based on the experimentally derived equations from Wang et al.,[25] This is shown as Eq. 1, which correlates the Vickers hardness H_V in MPa to yield strength, σ_{YS}, also in MPa. This correlation was chosen as the hardness and yield strength values in Ref. [25] are in the same range as the ones of René 41:[4,6]

$$H_V \approx (3.01 \pm 0.07) \bullet \sigma_{YS} \qquad (1)$$

Thermodynamic and Kinetic Simulations

Thermodynamic and thermokinetic simulations were conducted using the MatCalc simulation software package (http://matcalc.at; version 6.04 release 0.111). For equilibrium simulations, the desired input composition and phases of interest were selected. The predicted stable phases were

Table II. Wyckoff designations, resulting relative multiplicities, and used relative multiplicities of metal (*M*) and interstitial (*I*) sites in the crystal structures compared to their thermodynamic descriptions for M₆C and M₂₃C₆. These thermodynamic descriptions are used in the MCNI1 (original) and the TCNI9 databases. The correct crystallographic multiplicities are used in the modified databases MCNI2a and MCNI2b

M_6C				
Wyckoff designation	48f	32e	16d	16c
Site type (M, I)	M	M	M	I
Crystallographic site multiplicity	3	2	1	1
Multiplicity description in MCNI1 and TCNI9	2	2	2	1
$M_{23}C_6$					
Wyckoff designation	48 h	32f	24e	8c	4a
Site type (M, I)	M	M	I	M	M
Crystallographic site multiplicity	12	8	6	2	1
Multiplicity description in MCNI1 and TCNI9	20		6	3	

then evaluated as a function of temperature over a range from 600 to 1600 °C. In most of the simulations, Ni, Cr, Co, Mo, Al, Ti, Fe, C, B, and N were included. In the benchmarking calculations for Waspaloy, Zr was included as well. All the remaining elements are considered to be impurities and, thus, were discarded. The results were compared to simulations using the commercial TCNI9 database (v.9.1) in ThermoCalc. The equilibrium simulations were evaluated based on the phase stability regions as well as the phase compositions.

In the kinetic simulations, the initial condition was approximated using an equilibrium calculation at 1200 °C. Only the matrix γ phase and Ti-rich M(C,N)-type carbonitrides were predicted to be stable in René 41 at this temperature. In accordance with experimental observations, an M(C,N) precipitate population with a size distribution from 0.5 to 1.5 μm was generated, and the phase fraction of these precipitates was set to the equilibrium M(C,N) fraction at 1200 °C. γ' precipitates were set up as homogeneous precipitates with an initial phase fraction of 0%. To approximate the diffuse interface between the γ' precipitates and the matrix, the regular solution-critical temperature model, as implemented in MatCalc, was used with the critical temperature being set to 2500 K.[26] Additionally, the diffusion enhancement coefficients for both substitutional and interstitial elements with respect to the γ' precipitates were changed from the default value of 1–0.2, which yielded a good prediction of the precipitate size, as can be seen in the supplementary figures Fig. S-1, S-2, and S-3 (refer to online supplementary material). The adjustment of the diffusion enhancement coefficients are reasoned on the basis that the default value of 1 strictly applies to dilute solutions[27] and, thus, does not apply to René 41, as the γ' phase fraction exceeds 10%.[3] The M₆C and M₂₃C₆ carbides were introduced as grain-boundary precipitates with initial phase fractions of 0%. In the simulations, an initial mean grain diameter of 200 μm was selected to approximate the as-received grain size. Using this setup, a simulated

initial heat treatment of isothermal holding at 1200 °C for 0.5 h followed by cooling at a rate of 200 °C s⁻¹ was applied. The condition after this simulated heat treatment was then used as the starting point for all following simulations.

The heating curves for the kinetic simulations were approximated based on the assumption that the heat transfer from the furnace to the sample occurred by radiation. Based on an assumed sample geometry of a cube with 1-cm side length, the absorbing surface was assumed to be 6×10^{-4} m² and the density as 8250 kg m⁻³, as reported in Ref. 4. The heat capacity was approximated using a linear fitting curve based on literature data.[4,6] Despite the Ar atmosphere, the samples still exhibited slight surface oxidation. As the reflectivity of these surface oxides was unknown, the reflectivity/emissivity of the samples was assumed to be equal to 1. The temperature was then numerically approximated using the Stefan Boltzmann law of radiation.[28] Resulting exemplary time-temperature profiles can be seen in Fig. 1b. The curves were approximated up to 100 h. A level of 95% of the absolute target temperature was reached between 85 and 230 s according to these approximations, with shorter times associated with higher target temperatures.

The thermodynamic databases used for simulations in MatCalc were the openly available MC-NI database (v.2.034), designated here as MCNI1. This database was modified to improve the thermodynamic descriptions. The modified database that we developed contains the improved crystallographic descriptions of M₆C and M₂₃C₆ and is labeled MCNI2a. The further fine-tuned database using the experimental data is MCNI2b. The improvements in crystallographic descriptions of the thermodynamic database can be understood based on Table II, which shows the physical description based on the Wyckoff designations of the metal (M) and interstitial (I) sites for M₆C and M₂₃C₆, respectively. The available databases MCNI1 and TCNI9 use simplified descriptions that do not reflect the true crystallographic site multiplicities. This

has been corrected in the improved MCNI2a and MCNI2b databases.

Yield Strength Evaluation of Simulation Data

Descriptions for the strengthening of superalloys by γ' precipitates are derived in.[1] The change in the critical resolved shear stress, $\Delta\tau_{CRSS}$, for weakly coupled dislocations by coherent γ' precipitates is described as a function of the precipitate diameter, d, volume fraction, f, and anti-phase boundary energy, Γ_{APB}, in Eq. 2, where the Burgers vector, b, and shear modulus, G, are scaling parameters. In this case, the spacing between dislocations is large compared to the precipitate size:[1]

$$\Delta\tau_{CRSS} = \frac{\Gamma_{APB}}{2 \bullet b} \left[\left(\frac{6 \bullet \Gamma_{APB} \bullet f \bullet d}{2 \bullet \pi \bullet \frac{1}{2} \bullet G \bullet b^2} \right)^{\frac{1}{2}} - f \right] \quad (2)$$

For sufficiently large d or for antiphase boundary energy Γ_{APB} increases, the spacing between dislocations is of the same order as the γ' precipitate size. In this case, the behavior changes to that of strongly coupled dislocations, which is described in Ref. 1:

$$\Delta\tau_{CRSS} = \sqrt{\frac{3}{2}} \bullet \frac{2 \bullet G \bullet b}{d} \bullet f^{\frac{1}{2}} \bullet \frac{w}{\pi^{\frac{3}{2}}} \bullet \left(\frac{\pi \bullet \Gamma_{APB} \bullet d}{w \bullet G \bullet b^2} - 1 \right)^{\frac{1}{2}} \quad (3)$$

where w is a dimensionless parameter of the order of unity that will be assumed to be equal to 1 in the following.[1]

Both Eqs. 2 and 3 predict increasing strength with increasing volume fractions of γ' precipitates at a rate of $f^{\frac{1}{2}}$. However, Eq. 2 predicts an increase of the strengthening effect with larger precipitate diameters with approximately $d^{\frac{1}{2}}$, while Eq. 3 predicts a decrease with approximately $d^{-\frac{1}{2}}$. For even larger precipitates, another transition in the γ' precipitate–dislocation interaction takes place when Orowan looping becomes energetically favorable.[29] In this mechanism, instead of cutting the precipitates, the dislocations bend around them. The resulting strength increase is formally approximated by Eq. 4 and compared to the other strengthening factors, scales with d^{-1}:

$$\Delta\tau_{CRSS} = \frac{2 \bullet G \bullet b \bullet \sqrt{f}}{d} \quad (4)$$

The effective strengthening is always minimized, so that whichever mechanism results in the lower strength increase will be dominant.[1] Using these equations, the increase in shear stress can then be estimated assuming that the highest Schmid factor is the relevant scaling term between the increase in τ_{CRSS} and σ_{YS}, leading to:[30]

$$\Delta\sigma_{YS} \approx \Delta\tau_{CRSS} \bullet 2 \quad (5)$$

Visualization of Simulation Results

Data visualization of the experimentally generated TTP diagram regarding both the presence of M_6C and $M_{23}C_6$ precipitates as well as the hardness evolution in René 41 has been plotted using the OriginPro software. The contour plots depicting the simulated TTP data or precipitate size and fraction, as well as the evaluated expected yield strength increase based on the mathematical models in the previous section, were generated using Python (JupyterLab 3.2.1). To enable better data representation, a numerical interpolation of the simulated data was required to minimize distortion at short timescales and errors due to visualization artefacts. This interpolation was executed using Python's RBFInterpolator (Radial basis function interpolator) as implemented in the SciPy module (v.1.8).[31] Visual outputs were generated using the matplotlib (v. 3.5.1) module.[32]

RESULTS AND DISCUSSION

The experimentally gained insights are presented here and discussed. These are then applied to improve the thermodynamic descriptions of currently available databases. The modified database is used to simulate TTP diagrams, which are compared to experimental TTP diagrams. To establish the wider applicability of the improved database, it is tested on other alloys, and the results are compared to literature data.

Experimental Time–Temperature–Precipitation Data

Based on microscopy insights coupled with knowledge from previous publications,[13,17,18] the development of the experimental M_6C and $M_{23}C_6$ TTP diagrams for René 41 is described in the following. Figure 2 shows selected micrographs of samples after solutionizing and subsequent 10-h annealing at temperatures between 850 °C and 1150 °C. The bright phase is Mo-rich M_6C, the intermediate contrast phase is Cr-rich $M_{23}C_6$, and the dark phase is Al- and Ti-rich γ', as previously identified in Ref. 13.

After 10 h of annealing at 1150 °C (Fig. 2a), no secondary precipitates can be seen, although some primary M(C,N) type carbonitrides are visible (marked by red arrows). After annealing at 1100 °C (Fig. 2b), grain boundary M_6C is observed (white arrows), while no other secondary precipitates can be seen. Figure 2c shows M_6C and γ' precipitates at the grain boundaries after annealing at 1050 °C. Figure 2d, e and f shows M_6C, $M_{23}C_6$, (black arrows), and γ' precipitates at the grain boundaries at temperatures ≤ 1000 °C. Furthermore, γ' precipitates in the matrix have formed after 10 h of annealing between 900 and 1050 °C.

Although grain-boundary precipitates are observed after annealing at 900 °C (Fig. 2f) and 850 °C (Fig. 2g), they are not clearly distinguishable
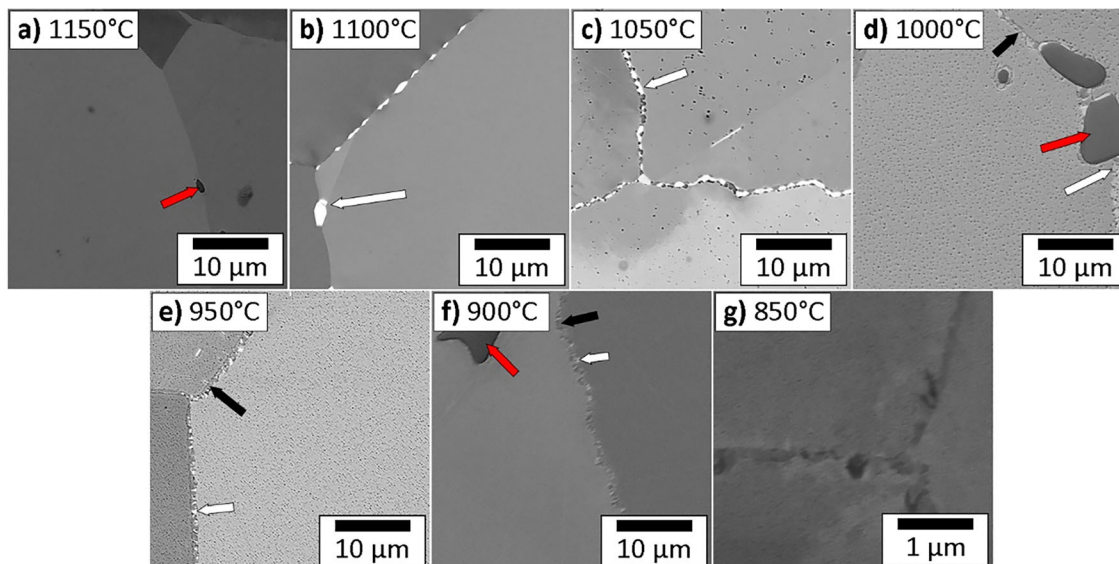
Fig. 2. SEM micrographs of grain boundaries from René 41 samples annealed for 10 h at (a) 1150 °C, (b) 1100 °C, (c) 1050 °C, (d) 1000 °C, (e) 950 °C, (f) 900 °C, and (g) 850 °C. *White arrows* indicate M_6C, *black arrows* $M_{23}C_6$ grain boundary precipitates, and *red arrows* M(C,N) carbonitrides (Color figure online).

from each other due to their small size. However, our previous work unambiguously confirmed M_6C, $M_{23}C_6$, and γ' precipitates at this temperature.[13] Micrographs for samples annealed at even lower temperatures are similar but not presented here.

The relative occupancy of grain-boundary carbides combined with the grain boundary length density were used to quantify the overall phase fraction of these carbides. Figure 3 shows the evolution of grain-boundary precipitate (a) volume fractions and (b) diameters after 10 h of annealing at various temperatures. The γ' results only include data of grain boundary γ' and not of intragranular γ'. Additionally, Fig. 3c and d presents the volume fractions and diameters for different isothermal holding times at 1000 °C. The corresponding data are provided in the supplementary Tables S-I and S-II. Figure 3a and b shows that the M_6C and grain boundary γ' precipitate diameters are in the order of 1–2 μm above 1000 °C, while, at lower temperatures, their diameters decrease to 400–500 nm. Generally, the diameters of the measured grain boundary precipitates are similar. However, the diameters of the $M_{23}C_6$ precipitates may be misjudged. These precipitates are often adjacent to each other, making it difficult to determine where one precipitate ends and the next begins. Notably, the amount of $M_{23}C_6$ precipitates at the grain boundaries is higher than the M_6C content by a factor of about 2–3, which corresponds to the faster precipitation kinetics of $M_{23}C_6$ compared to M_6C, as also reported in Haynes 282.[33] Under isothermal conditions at 1000 °C (Fig. 3c and d) the phase fractions and diameters of all the observed precipitates increase across the observed timescale from 0.1 to 10 h, although the $M_{23}C_6$ precipitate growth

kinetics appear to slow down somewhat between 1 and 10 h of isothermal holding.

Based on the combination of results presented here and from Ref. 13, the isothermal TTP diagram in Fig. 4 was developed. The kinetics of $M_{23}C_6$ and M_6C precipitation were not directly distinguishable, although a faster precipitation rate of $M_{23}C_6$ has previously been reported.[33] In some cases, grain-boundary precipitates were visible, but they were so small that neither their composition nor their contrast yielded enough information for a clear distinction between them (shown in gray). Based on their position within the time–temperature region, it can be reasoned that these precipitates are likely $M_{23}C_6$ and M_6C, as previously confirmed.[13] At temperatures below 750 °C, no grain-boundary precipitates were detected after 10 h of annealing.

Modification of the Thermodynamic Database Based on Experimental Results

Thermodynamic Phase Stability and Carbide Composition

Comparing the experimental observations from the previous section and previous studies (Fig. 5a),[17,18] to equilibrium simulations with currently existing thermodynamic databases (Fig. 5b and c) reveals discrepancies in the stability regions of M_6C and $M_{23}C_6$. The experimental data in the present study put the M_6C solvus between 1100 °C and 1150 °C, and the $M_{23}C_6$ solvus between 1000 °C and 1050 °C. The data by Collins[18] confirm the M_6C solvus temperature as 1147 °C, but report a lower $M_{23}C_6$ solvus between 926 °C and 982 °C, as shown in Fig. 5a.
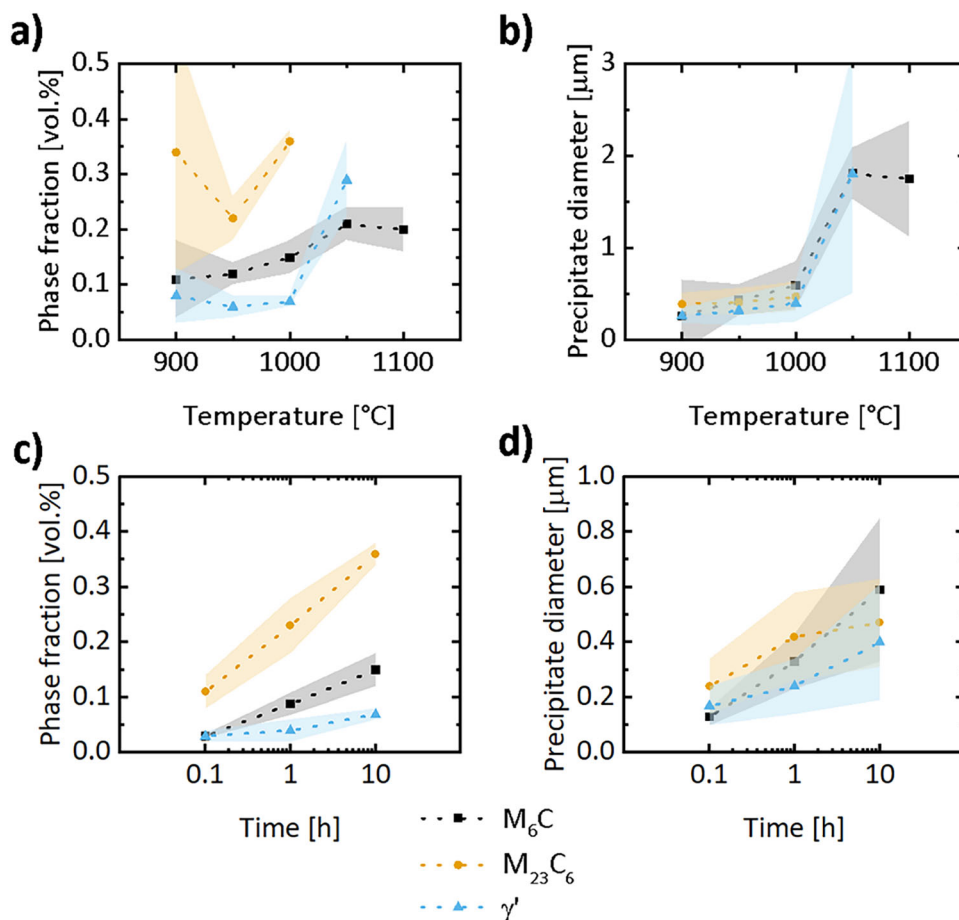
Fig. 3. Evolution of experimentally observed grain boundary precipitates M_6C (in *black*), $M_{23}C_6$ (in *yellow*), and grain boundary γ' (in *blue*). (a) and (b) the phase fraction and diameter after 10 h of annealing between 900 and 1100 °C, respectively. (c) and (d) the evolution of the precipitate fraction and diameter during annealing at 1000 °C on double-logarithmic scales, respectively. The *shaded areas* indicate standard deviations (Color figure online).

In comparison, the predicted M_6C solvus temperatures in the MCNI1 (Fig. 5e) and TCNI9 (Fig. 5c) databases are 996 °C and 945 °C, respectively. When including the topologically closed packed (TPC) σ phase, both databases predicted that M_6C is not thermodynamically stable, as displayed in Fig. 5b and d. For $M_{23}C_6$, the predicted stability range is appropriate, with predicted solvus temperatures of 962 °C and 967 °C for the MCNI1 (Fig. 5e) and TCNI9 (Fig. 5c) database, respectively.

Due to these discrepancies, the MCNI1 database was updated with more accurate thermodynamic descriptions. The equilibrium simulations from the first update of the thermodynamic database, i.e., the MCNI2a database, can be seen in Fig. 5f and g. This database includes the improved crystallographic description of these carbides, correcting the relative multiplicities, as described in Table II. The phase fraction diagrams show that the stability of these carbides is improved, e.g., M_6C is stable even with included TCP phases. However, when comparing the results to the experimental data from Collins[18] (Fig. 5a), the stabilities of both carbides are now overestimated.

Therefore, a finetuning step of the database was applied. This was done by iteratively adjusting the thermodynamic description of M_6C and $M_{23}C_6$ in the MCNI2a database until a good match was achieved between simulation and experiments with respect to both the solvus temperatures and chemical compositions of these carbides. The stability range of the updated database, MCNI2b, is shown in Fig. 5h and i. This database now yields stability ranges that match both, those predicted by Collins[18] as well as the experimentally observed TTP data in the present study.

Additionally to the phase stability range, the phase compositions can also be used as a measure of the quality of the thermodynamic database. Table III compares the simulated compositions of M_6C at 1100 °C from the TCNI9, MCNI1, and MCNI2b databases to experimental atom probe microscope (APM) data from Ref. 13. The APM data were collected after annealing for 10 h at 1100 °C. The average error column shows the averages of the deviations between simulated and APM chemistries for the considered elements. Elements not included
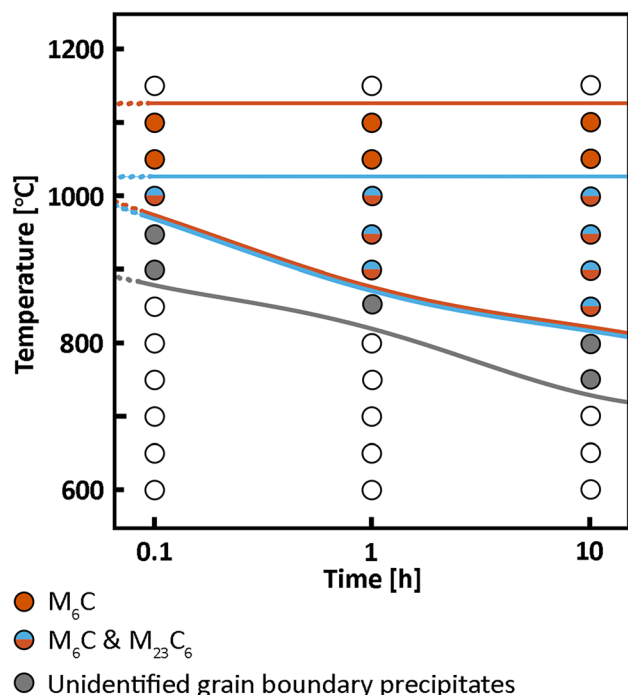
Fig. 4. TTP diagram based on SEM and EDS data, indicating the presence of M_6C (*red*) and $M_{23}C_6$ (*blue*) at the grain boundaries. Additionally, the data points, where grain-boundary precipitates were present but not unambiguously identifiable are shown in *gray*. O*pen circles* no grain boundary precipitates were detected (Color figure online).

in the database or not detected in the APM results are omitted from this analysis.

The errors in the TCNI9 and MCNI1 databases are larger than those for the MCNI2b database by a factor of ∼ 2. These errors can be associated with differences in the simulated and observed Mo concentration. Notably, neither of these databases predicted stable M_6C at this temperature. However, there is still a theoretical composition output of the 'most stable' variant of M_6C provided. The MCNI2b database generates a smaller error than the databases with the simpler crystallographic phase descriptions. The difference between kinetic and equilibrium simulations is negligible. Notably, only the modified MCNI2b database includes data for the Ti solubility, as pointed out in Ref. [13], while it does not include data for the Fe solubility.

In analogy to the results for 1100 °C, the results for 900 °C are presented in Table IV.[13] Here, the equilibrium simulation based on the TCNI9 database shows the largest compositional error. These errors are associated with deviations in Co and Mo content from the experiment. For the MCNI1 database, the simulated Mo-content is also wrongly predicted in the equilibrium and kinetic simulations. These elements are, again, correctly simulated in the modified MCNI2b database. However, the MCNI2b database overestimates the Cr-content in the equilibrium compared to the APM data but yields more accurate results for the kinetic

simulations. As the APM sample was not in an equilibrium condition, these kinetic simulations reflect the material's condition better.

In analogy to M_6C, the composition of $M_{23}C_6$ carbides at 900 °C are presented in Table V.[13] In general, the observed differences between experiment and simulation are smaller for $M_{23}C_6$ than those observed for M_6C. TCNI9 predicts a higher Cr content than the observed one, while MCNI1 shows a higher Ni content. All the databases reflect the experimental Mo content well.

The B content of $M_{23}C_6$ in the thermodynamic MCNI1 and MCNI2b simulations is well predicted. However, the kinetic simulations underestimate the B content. This can be attributed to the strong segregation tendency of B to high-angle grain boundaries in Ni.[34,35] There is no description of such segregation effects implemented in the simulation model used in the present study. This leads to a lower B-content in the vicinity of grain boundary $M_{23}C_6$ in the simulation compared to physical reality, expressing itself as a reduced B-content in simulated $M_{23}C_6$. Notably, TCNI9 does not include a description of the substitution of C by B.

In summary, the composition of $M_{23}C_6$ and M_6C (Tables III, IV, and V) are improved in the MCNI2b database, compared to the older databases without updated thermodynamic descriptions. This confirms that the updated database provides improved quantitative outputs with respect to the M_6C and $M_{23}C_6$ carbides in René 41.

Precipitation Kinetics of Carbides

Although the previous section has already evaluated the chemical compositions of $M_{23}C_6$ and M_6C in kinetic simulations, the focus of this section will be on assessing their precipitation kinetics in more detail.

Figure 6a, b, c and d shows the simulated TTP diagrams for $M_{23}C_6$ carbides using the MCNI1 and modified MCNI2b databases. The TPP diagrams for $M_{23}C_6$ are qualitatively similar for both databases. However, the MCNI2b results predict higher precipitate fractions and diameters than the MCNI1 database. This indicates faster precipitation and coarsening kinetics, which better represent the experimental observations from Fig. 3. The change in M_6C precipitation behavior between the databases is larger as displayed in Fig. 6e and f. The MCNI1 database (Fig. 6e and g) shows the fastest precipitation kinetics at about 950 °C and the stability of M_6C up to 1000–1050 °C. In the MCNI2b database (Fig. 6f and h), the fastest kinetics are shifted to approximately 1050 °C with a stability range up to 1100–1150 °C. Thus, the modified MCNI2b database also reflects the experimental observations (Fig. 3) for M_6C better than the original one.

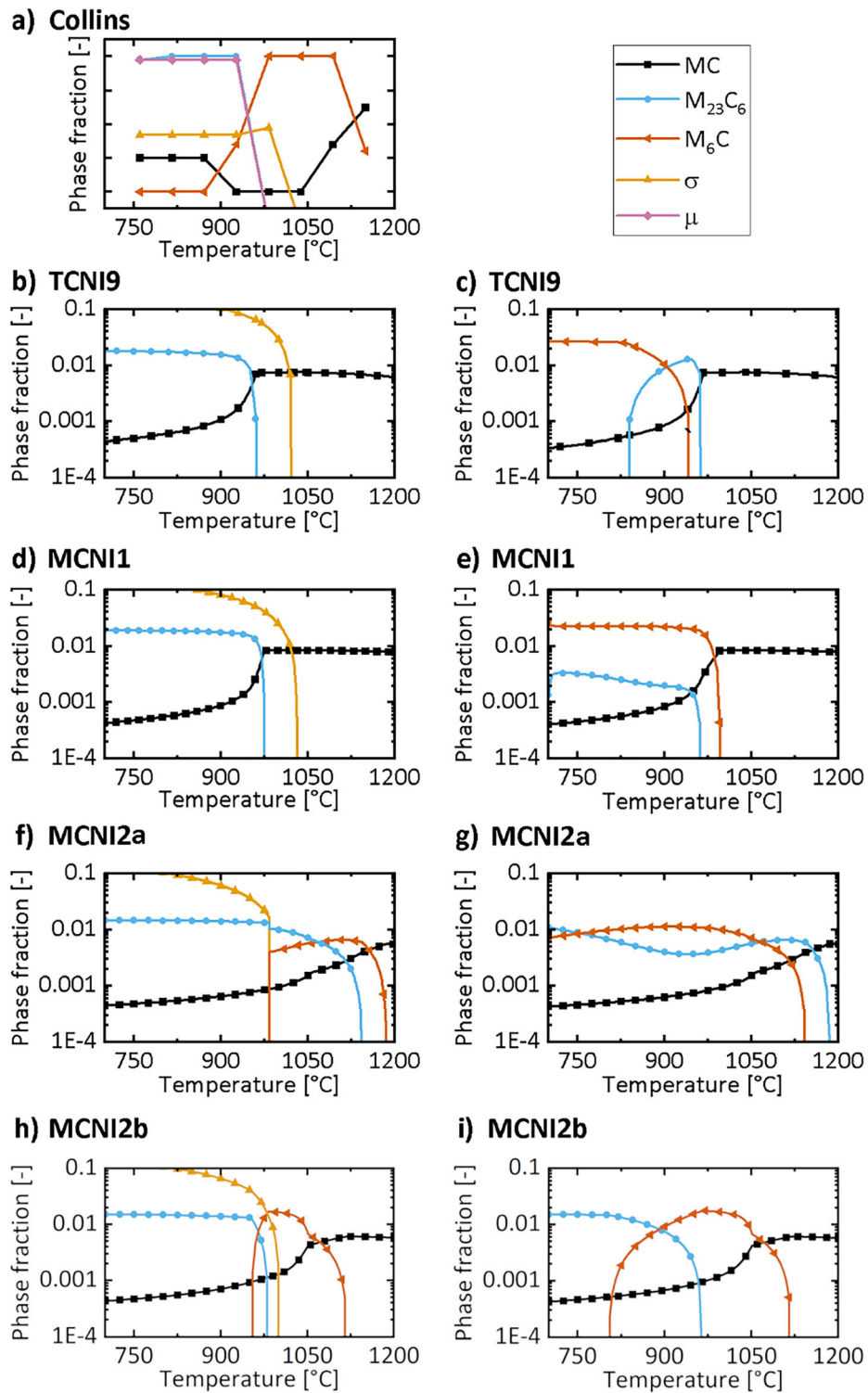To enable an easier quantitative comparison of the simulation data to the experimental

Fig. 5. (a) Experimental data for long-term isothermal holding of René 41, as reported by Collins.[18] (b) and (c) Equilibrium calculations based on the TCNI9 database with and without σ phase included in the simulation. (d) and (e) Equilibrium calculations based on the MCNI1 database with and without σ phase included. (f) and (g) Equilibrium calculations based on the modified MCNI2a database with and without σ phase included. (h) and (i) Equilibrium calculations based on the further improved MCNI2b database with and without σ phase included.

Table III. Composition of M_6C in thermodynamic equilibrium simulations at 1100 °C using the TCNI9, MCNI1, and modified MCNI2b databases, compared to the kinetic simulation results (after 10 h isothermal holding) from the MCNI2b database and experimental APM data from Ref. 13

Data source	Database	Element								Average Error
		Ni	Co	Mo	Cr	Ti	C	Fe	
		[at.%]							[at.%]
Thermo-dynamic	TCNI9[b]	26.8	2.2	37.9	17.8	-	14.3	1.0	5.44±4.7
	MCNI1[b]	19.2	10.8	35.5	19.4	-	14.3	0.8	4.5±4.1
	MCNI2b[a]	23.5	8.2	27.5	20.9	5.6	14.3	-	1.8±1.4
Kinetic	MCNI2b[a]	24.0	7.6	28.0	20.3	5.7	14.3	-	1.9±1.5
APM		22.5	7.1	22.7	22	8.2	15.3	0.7	

Shading represents the absolute error in the composition prediction from 0 (white) to 10 (red). The average error column shows the averages of the deviations between simulated and APM chemistries for the considered elements[a]These databases do not predict stable M_6C at this temperature, however, there is still a theoretical composition output of the 'most stable' variant of M_6C provided[b]The MCNI2b database includes the improved crystallographic phase descriptions

observations, Fig. 7 shows selected datapoints from the kinetic simulations using the original MCNI1 and modified MCNI2b database. These simulation results can be directly compared to experimental data shown in Fig. 3. The MCNI1 database (Fig. 7a and b) underestimates the phase fractions and stability ranges of both $M_{23}C_6$ and M_6C. Contrary, the stability range as well as phase fractions of both carbides are matched well between the experiment and the simulations from the MCNI2b database (Fig. 7c and d).

At low temperatures of < 1000 °C, simulations with both databases lead to 4–6 times larger precipitate diameters than experimentally observed. This may be a consequence of a possibly overestimated matrix-precipitate interface energy, as well as interactions between the M_6C and $M_{23}C_6$ carbides at the grain boundaries, which are not included in the simulation model. Due to lack of available literature data regarding these interfacial energies, no attempts were made to correct this issue in the simulations here.

Evaluation of γ' Precipitation Kinetics

The previous sections established that the modified MCNI2b database results in improved thermodynamic and kinetic simulations of $M_{23}C_6$ and M_6C carbides. However, as intragranular γ' are the dominant strengthening precipitates in Ni-based superalloys, any modification made on a database must include an accurate description of this phase. Thus, this section will evaluate if the modified MCNI2b database yields correct γ' results that agree with experimental observations.

Figure 8 presents kinetic simulation results for γ' precipitates for MCNI1 and MCNI2b databases. There are no significant differences between the results using those two databases. This is expected, as the thermodynamic description of γ' has not been changed. The high phase fraction of γ' precipitates even at low times is due to significant amounts of γ' precipitates predicted during the initial quenching simulation. The precipitation during quenching leads to approximately 16 mol% γ' precipitates with mean diameters of approximately 1–2 nm.

Table IV. Composition of M_6C as evaluated for thermodynamic equilibrium simulations at 900 °C using the TCNI9, MCNI1, and modified MCNI2b databases, compared to the kinetic simulation results (after 10 h isothermal holding) from the MCNI1 and MCNI2b database and experimental APM as evaluated in Ref. 13

Data source	Database	Element Ni [at.%]	Co	Mo	Cr	Ti	C	Average Error [at.%]
Thermo-dynamic	TCNI9	26.8	1.71	37.8	18.6	-	14.3	5.2±2.8
	MCNI1	21	8.7	35.2	18.7	-	14.3	2.7±1.9
	MCNI2b[a]	21.5	9.9	26.9	24.9	2.4	14.3	2.2±0.9
Kinetic	MCNI1	23.4	7.1	34.4	21.3	-	14.3	2.8±2.0
	MCNI2b[a]	24.2	6.4	29.8	20.2	5.2	14.3	1.9±1.7
APM		18.5	8.4	29.2	21.4	4.1	15.3	

Shading represents the absolute error in the composition prediction from 0 (white) to 10 (red). The average error column shows the averages of the deviations between simulated and APM chemistries for the considered elements[a]The MCNI2b database includes the improved crystallographic phase descriptions

Experimentally determined intragranular γ' precipitate diameters and phase fractions after 10 h of annealing are shown in Fig. 9. The precipitate size in Fig. 9a decreases following a near-linear trend across the studied temperature range. With decreasing temperature, this quantitative analysis becomes more inaccurate, as reflected by the increasing width of the error bar (Fig. 9b).

Although γ' precipitates are visible within the matrix after 10 h of annealing at temperatures below 850 °C, these precipitates were too small for a reliable quantification. Therefore, an indirect approach was used to analyze them based on the strengthening effect of γ' precipitates in René 41. The increase in yield strength during annealing based on Vickers hardness measurements is shown in Fig. 10a. This figure shows a trend for the time-temperature-hardening behavior roughly in line with a previous report on René 41.[3] The hardness values are shown in the supplementary Fig. S-4.

The strength–hardness correlation described in Eq. 1, as derived in Ref. 25, is used in the following to calculate an estimated yield strength of the material. The contour map in Fig. 10a shows a pronounced strength maximum after ageing for 10 h at around 850 °C. At temperatures above 800 °C, the peak hardness is shifted to shorter times, followed by a decrease in hardness due to over-ageing of the strengthening γ' precipitates. This is associated with the transition of the dislocation-precipitate interaction from weak to strong coupling.[1] At temperatures below 800 °C, the precipitation kinetics and size evolution of γ'

Table V. Composition of $M_{23}C_6$ as evaluated for thermodynamic equilibrium and kinetic simulations at 900 °C using the TCNI9, MCNI1, and modified MCNI2b databases, compared to the kinetic simulation results (after 10 h isothermal holding) from the MCNI1 and MCNI2b databases and averaged APM results as measured in Ref. 13

Data source	Database	Element								Average Error
		Ni	Co	Mo	Cr	Ti	C	B	Fe	
		[at.%]								[at.%]
Thermo-dynamic	TCNI9	2.5	0.8	9.6	66.1	-	20.7	-	0.2	4.3±3.4
	MCNI1	10.3	1.8	8.6	58.5	-	18.5	2.2	0.1	2.6±1.5
	MCNI2b[a]	8.7	4.5	10.3	53.5	2.2	18.2	2.5	-	1.3±0.7
Kinetic	MCNI	9.9	1.6	8.8	59	-	20.5	0.1	0.1	3.1±1.6
	MCNI2b[a]	7.1	3.2	10.3	54.5	4.1	20.5	0.2	-	1.4±1.5
APM		7.3	3.2	11.7	53.7	4.3	15.9	3.2	0.7	

Shading represents the absolute error in the composition prediction from 0 (white) to 10 (red). The average error column shows the averages of the deviations between simulated and APM chemistries for the considered elements[a]The MCNI2b database includes the improved crystallographic phase descriptions

precipitates is slower, meaning that longer ageing times would be required to achieve the peak hardness.

The yield strength of γ'-free René 41 has been reported to be in the range of 440–500 MPa, which is higher than that of other γ'-free superalloys, such as Alloy 600 or Haynes 230.[6] This is attributed to the higher solute contents in the matrix of René 41 compared to other precipitate-free superalloys.[6] When considering the expected maximum strength of René 41 based on adding the strength of precipitate-free material and the maximum increase in yield strength, as determined from hardness test data, this yields a peak strength around 1 GPa, which is in line with the values reported in Ref. 4. This confirms that the used equations to calculate the yield strength increase yield accurate results.

To gain additional qualitative insights into the γ' precipitation behavior from the MCNI2b simulations, the γ' precipitate hardening was modeled using Eqs. 2–4. Γ_{APB} was evaluated according to the model proposed in Ref. 36, based on the contents of Mo, Ti, Al, Co, and Cr in γ' precipitates. The temperature dependence of the interaction coefficients was approximated using a parabolic function based on the individual datapoints reported in Ref. 36. For the resulting predicted increase in τ_{CRSS}, a

transition from weak to strong coupling is expected in the range of a few 10 nm, while the transition from strong coupling to Orowan looping likely takes place at around 100-nm precipitate diameters, both of which are roughly in accordance with values presented for Nimonic 105, PE 16,[1] and Udimet 720LI.[37] Converting these values into the predicted yield strength increase according to Eq. 5 leads to the time–temperature–strength diagram shown in Fig. 10b. This diagram shows a maximum increase in strength of about 676 MPa between 800 and 900 °C. The results of these simulations are in excellent agreement with the experimental results in Fig. 10a.

Benchmarking the Updated Database Against Other Alloys

The previous sections showed that the modified database more accurately simulates the stability ranges of M_6C and $M_{23}C_6$ carbides in René 41 than previously available CALPHAD databases. Further, it has been demonstrated that the stability range of γ' precipitates do not require additional adaptations. As the database was optimized for the description of René 41, this is to be expected. However, a wider applicability of this database will be established in the following based on literature reports about the
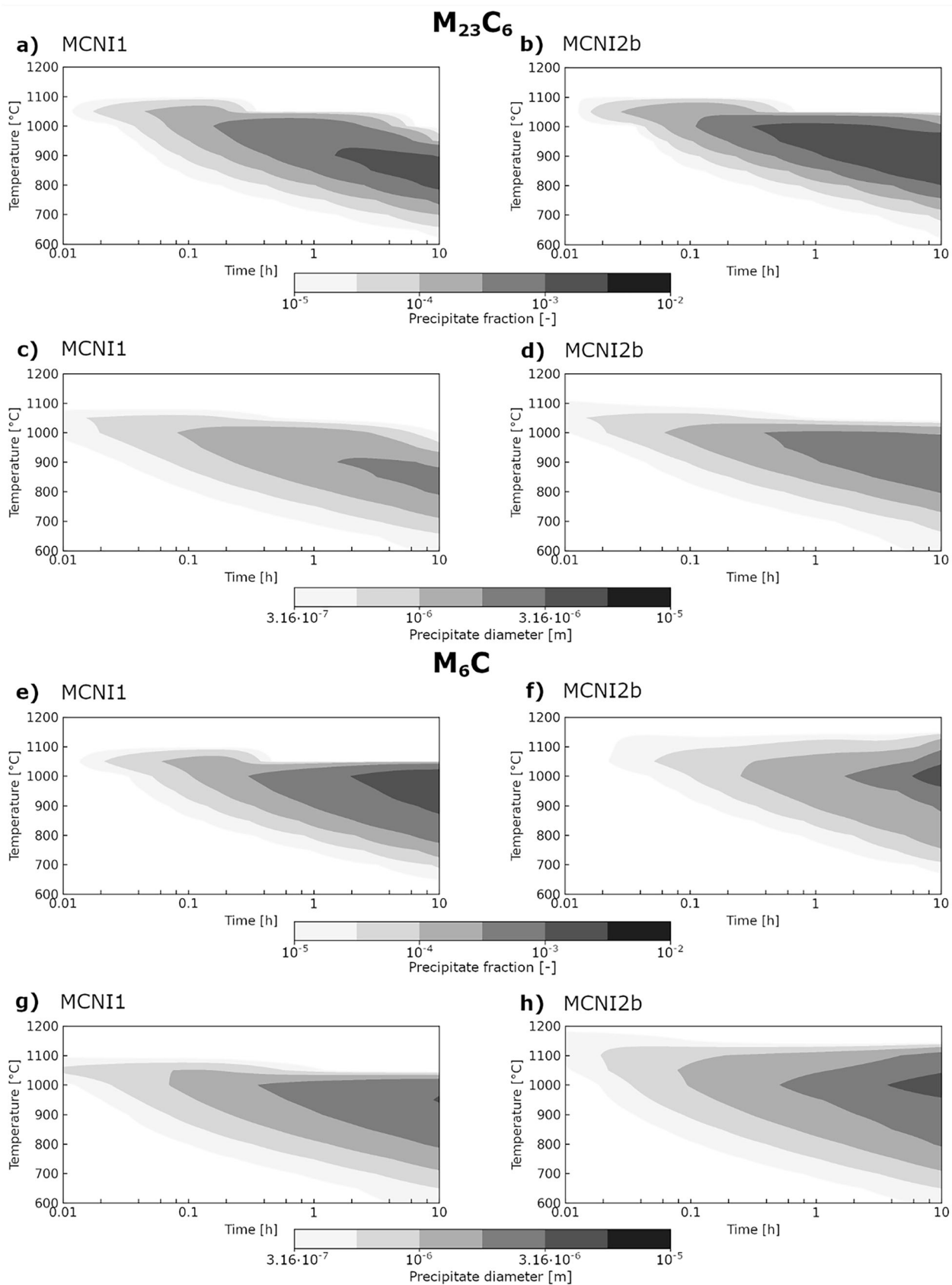
Fig. 6. Simulated TTP diagrams for (a–d) $M_{23}C_6$ and (e–h) M_6C for the original MCNI1 (*left column*) and modified MCNI2b (*right column*) databases. The respective *first rows* show molar phase fractions, while the *second rows* show precipitate diameters.
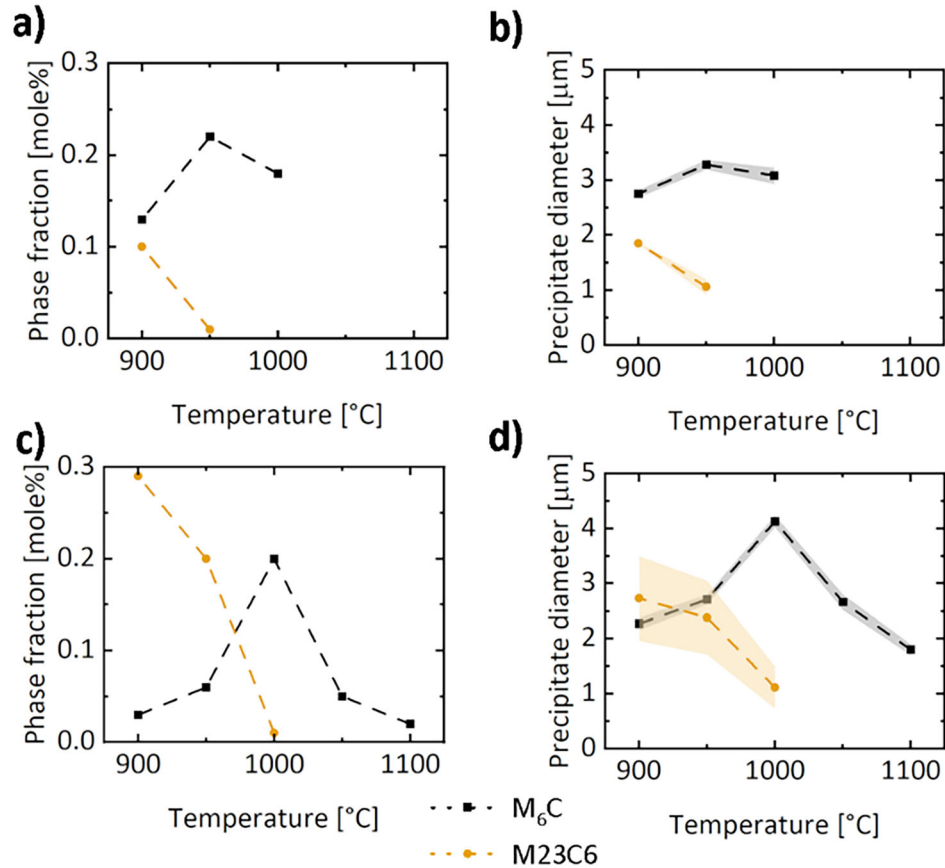
Fig. 7. Kinetic simulation results after 10 h annealing for the (a, b) MCNI1 database and (c, d) modified MCNI2b database. (a) and (c) show mole phase fractions and (b) and (d) show precipitate diameters.

stability ranges and compositions of $M_{23}C_6$ and M_6C carbides in other superalloys with similar compositions to René 41. Based on the availability of data, Waspaloy, Udimet 700, and Haynes 282 were selected to evaluate the thermodynamic stability range of the present phases as a function of temperature.[18,33] Further alloys were not included, as the current thermodynamic descriptions of M_6C and $M_{23}C_6$ in the MCNI2b database do not yet include data on W, V, Ta, and other common alloying elements in superalloys. Further, the MCNI MatCalc database does not include thermodynamic data of M_3B_2 borides, therefore, M_2B type borides were included instead. However, as both M_3B_2 and M_2B are Cr- and Mo-rich, this was deemed a suitable replacement in the simulations.[2]

Figure 11 presents experimental phase stability ranges reported in literature and compares them to the simulated results. The experimental Udimet 700 (Fig. 11a, b and c) and Waspaloy (Fig. 11d, e and f) data[18] show an excellent match with the modified MCNI2b database. The $M_{23}C_6$ solvus temperature of both alloys is underestimated in the original MCNI1 database, but is correctly simulated with the updated thermodynamic phase descriptions. The stability ranges of MC carbides and borides are unaffected by the changes made.

Fahrmann et al.,[33] reported an experimental TTP diagram for Haynes 282, which was used to extrapolate the stability ranges for M_6C and $M_{23}C_6$ carbides. The experimental solvus temperature for both carbides was found to be around 1100 °C, with phase stabilities down to 700 °C. The equilibrium simulations of Haynes 282 in Fig. 11g, h and i show that the MCNI1 database vastly underestimates the stability regions of both M_6C and $M_{23}C_6$ carbides. The modified MCN2b database yields good results for the $M_{23}C_6$ stability with a simulated solvus temperature of around 1149 °C. However, the M_6C stability at high temperatures seems to be overestimated, while its stability at low temperatures is underestimated. Thus, neither the originally available nor the updated database reflect its stability correctly. This shows that future work is required to simulate M_6C in Haynes 282. The chemical compositions of M_6C and $M_{23}C_6$ after isothermal holding at 100 h at 1038 °C and 982 °C respectively in Ref. 33 are compared to the equilibrium simulations in the supplementary tables Tables S-III–S-VI and show a comparable quality between the adjusted
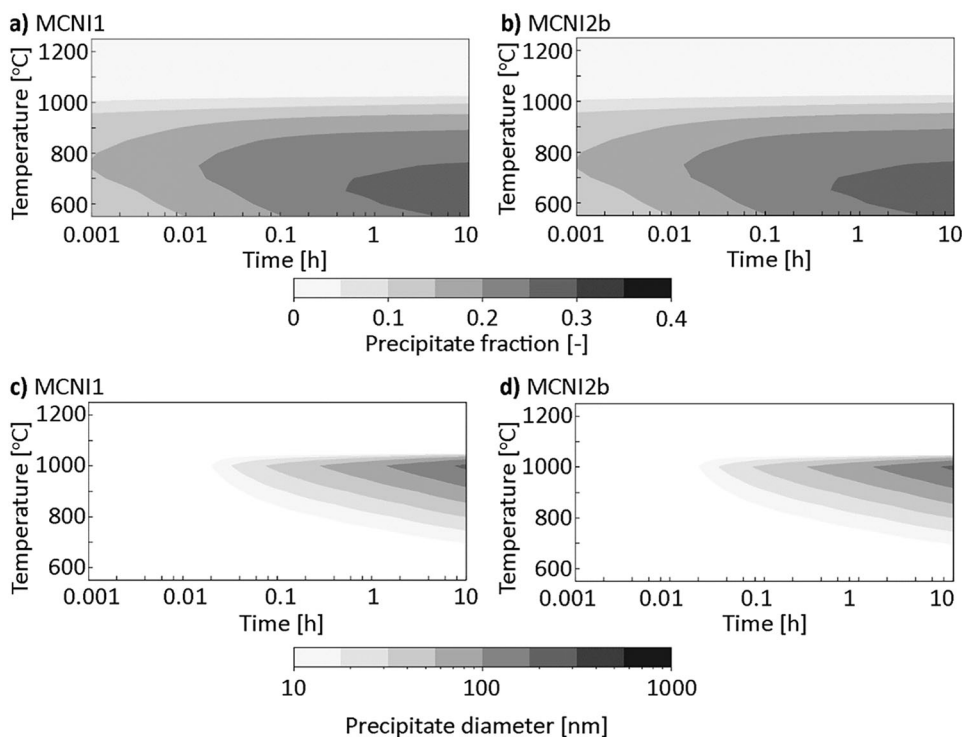
Fig. 8. γ' precipitate evolution for the original MCNI1 and modified MCNI2b databases. Molar phase fractions of γ' using the (a) MCNI1 and (b) MCNI2b databases and γ' precipitate diameters as predicted using the (c) MCNI1 and (d) MCNI2b databases. The resulting phase fractions and diameters are similar in both databases.
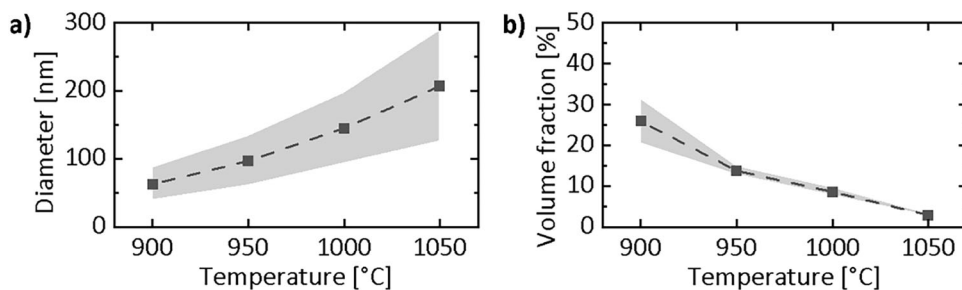

Fig. 9. Experimental evaluation of intragranular (a) γ' precipitate diameter and (b) γ' precipitate fraction after 10 h of heat treatments at the respective temperatures. The *gray shaded area* marks the standard deviation.

MCNI2b and the older TCNI9 and MCNI1 databases.

Additionally, the supplementary figure Fig. S-5a shows the experimentally observed carbides for different alloy compositions and (b), (c), and (d) shows equilibrium simulations at the same temperature across a wide range of compositions, as evaluated based on the TCNI9, MCNI1, and MCNI2b databases, respectively. In general, all three databases provide similar matches relative to the experimental data, with the MCNI1 and MCNI2b predicting a slightly higher stability of $M_{23}C_6$, as visible for the datapoint of 33.5 wt% Cr and 5.5 wt% Mo, where the experiments yielded both M_6C and $M_{23}C_6$, while simulations only indicated the stability of $M_{23}C_6$.

Therefore, the modified MCNI2b database yields either comparable or improved results for the tested superalloys, underpinning that the MCNI2b database can be readily applied to other Ni-based superalloys. Importantly, the multi-site compound energy model for $M_{23}C_6$ contains higher complexity in terms of CALPHAD parameters to be optimized than previous simplification. However, here, in the composition space of Ni-based superalloys, we can neglect Fe in the carbide formula as experimentally confirmed, which in terms of dissolution of elements once again represents a *chemical* simplification.
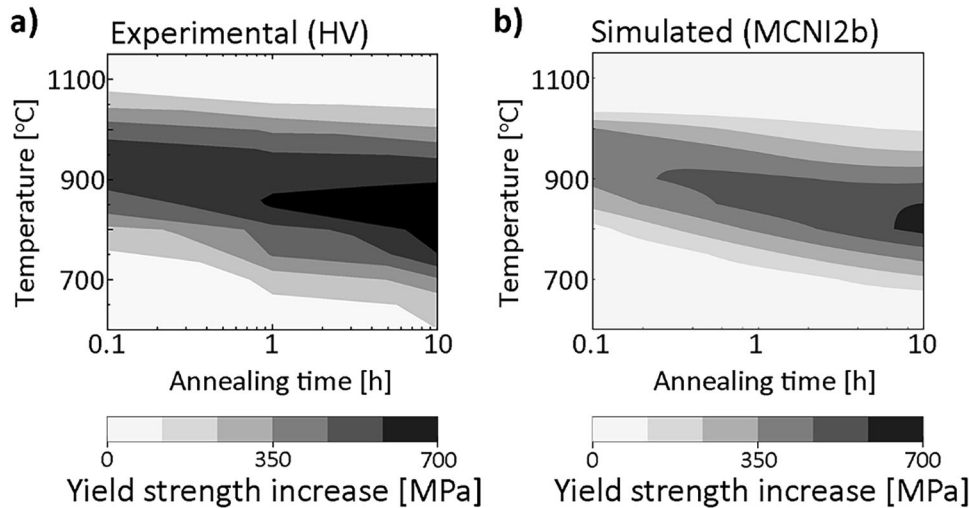
Fig. 10. (a) Contour map of yield strength increase during annealing calculated from the experimentally determined hardness using Eq. 1.[25] The minimum detected hardness of 1830 MPa, i.e., the hardness after solutionizing, was used as the reference for the increase in yield strength. (b) Increase in yield strength as predicted by the thermokinetic simulations using the modified MCNI2b database based on the γ' precipitate size and phase fraction when applied to Eqs. 2–5.[1,30]

This results in fewer end-member compounds and mixing interactions between various species of the phase to be assessed. Thus, we believe that we can base an appropriate model description of the phase on its carefully determined chemistry by our experiments, involving the relevant Ti solubility as here experimentally confirmed. This is further supported by the correct assessment of the solvus temperature of the Ni-based superalloy René 41. Generally, our experience (particularly the question of Si-solubility limits in various M_6C compound energy models[38]) has shown advantages of employing more physically modeling approaches in terms of size occupations. We hope that our approach, together with the new compound energy modeling of carbides, inspires a higher data density, including first-principles end-member energies, which will support future advancements in CALPHAD modeling of $M_{23}C_6$ and M_6C in Ni-rich high-alloyed material. It should be noted that our chemical simplification of no Fe in the carbide formula, therefore will not allow for a validation of Fe-Cr-C phases ($M_{23}C_6$ is indeed a stable phase in this subsystem) and, thus, the models can only be applied to Ni-based superalloys to date. Future modifications of the database aim to include Fe in the improved $M_{23}C_6$ description. However, this chemical simplification enhances the overall description and, we believe, facilitates a CALPHAD assessment of parameters of known ternary systems such as Mo-Cr-C[39] and Ni-Cr-C[40] (see also supplementary figure Fig. S-5).

SUMMARY AND OUTLOOK

A comparison of thermodynamic and kinetic simulations and experimental data demonstrated that currently available thermodynamic databases do not yield accurate results for describing the through-process evolution of carbides in René 41 and other similar Ni-based superalloys. Thermodynamic data and experimental results were successfully combined to improve the predictive quality of simulations for grain-boundary carbides M_6C and $M_{23}C_6$. The following findings were made:

- An experimental TTP diagram for René 41 was generated for the 0.1- to 10-h timeframes where $M_{23}C_6$ was found below 1000 °C and M_6C below 1100 °C. The nucleation sites of these carbides were identified as grain boundaries.
- Our modified thermodynamic MCNI2b database for MatCalc results in improved stability as well as improved compositional predictions for both M_6C and $M_{23}C_6$ carbides. This modified database shows a better predictive quality than the original version of the MCNI1 MatCalc database, as well as the TCNI9 (v.9.1) database available for ThermoCalc.
- It is shown that the description of the main strengthening phase γ' in the modified database remains correct. Kinetic simulations were able to successfully simulate c′ precipitation during annealing and were quantitatively related to the yield strength increase.
- Based on the experimental data available in the literature, equilibrium calculations using the modified database showed either comparable or improved results for other Ni-based superalloys with respect to M_6C and $M_{23}C_6$ carbide stability ranges.

The modified MCNI2b database is openly available under the name 'mc_ni_L.tdb' on https://www.matcalc.at/[19] and archived in Mendeley Data.[20] The updates in the thermodynamic database yields improvements in the predictive quality in the Ni-
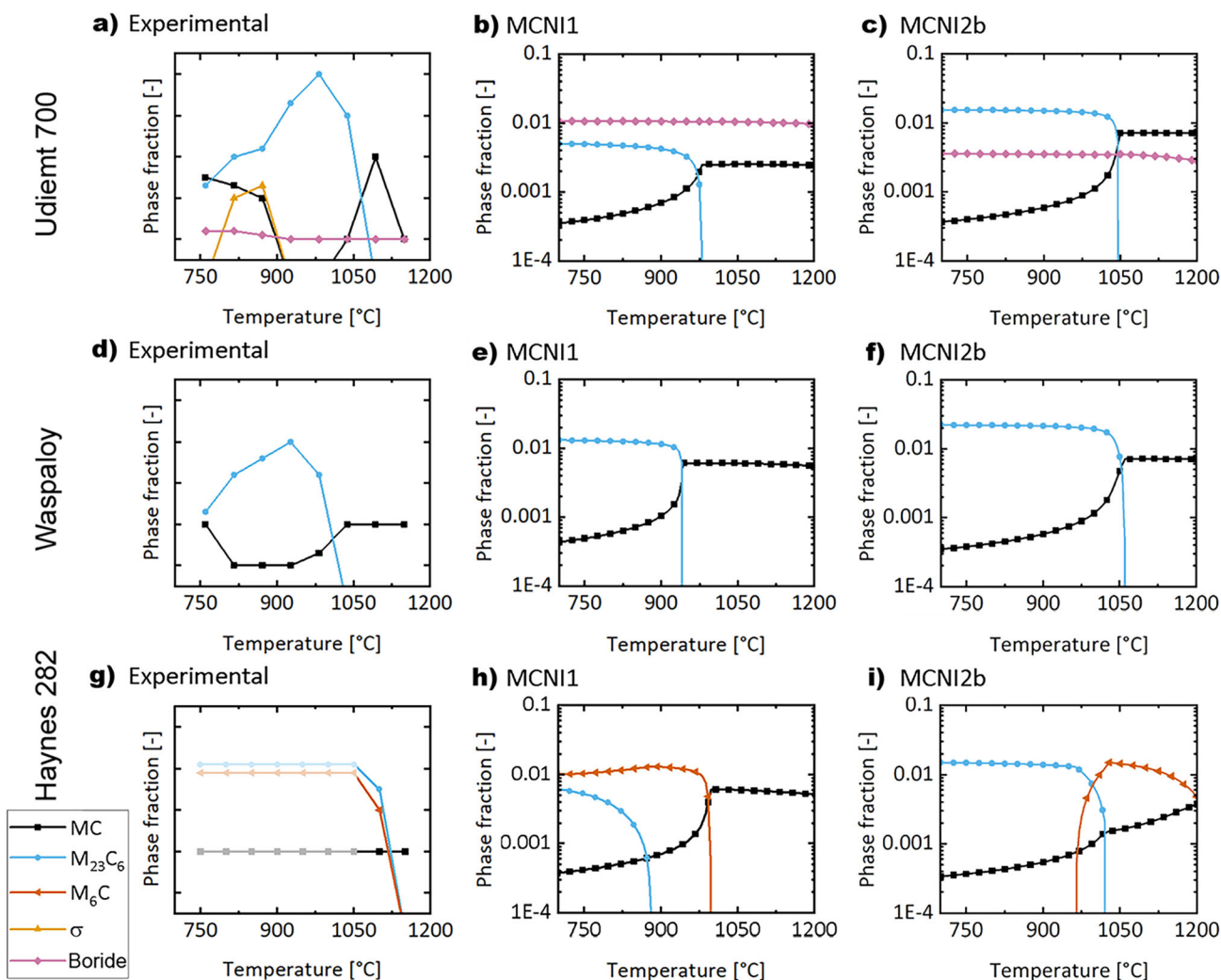
Fig. 11. Comparison of experimental equilibrium phase fraction diagrams (*first column*) with simulated diagrams based on the MCN1 database (*second column*) and the modified MCN2b database (*third column*) for (a–c) Udimet 700, (d–f) Waspaloy, and (g–i) Haynes 282. The thermodynamic experimental data for Udimet 700 and Waspaloy are reported in Ref. 18. The experimental solvus temperatures for Haynes 282 are extrapolated from the kinetic TTP diagram (up to 167 h) reported in Ref. 33 and, thus, the equilibrium phase fractions cannot be determined (as indicated by *faded colors*) (Color figure online).

Cr-Co-Mo-Al-Ti-C-B-N alloy design space. Improved predictive power with respect to phase stability and microstructural evolution are the results of these advancements. Such modeling capabilities are fundamental for designing thermomechanical processing and heat-treatment routes for aerospace and other high-performance applications. This will facilitate the creation of digital twins for superalloy products and accelerate the development of new alloys. However, the current version of the database does not consider several common elements in superalloys, such as W, Nb, Ta, V, or Fe in the description of the $M_{23}C_6$ and M_6C carbides. This underscores the need for future research to incorporate these alloying elements, as their inclusion would further enhance the applicability of these simulations.

CONFLICT OF INTEREST

The authors declare that they have no conflict of interest.

SUPPLEMENTARY INFORMATION

The online version contains supplementary material available at https://doi.org/10.1007/s11837-024-06484-8.

ACKNOWLEDGEMENTS

OPEN ACCESS

DATA AVAILABILITY

The modified MCNI2b database is openly available under the name 'mc_ni_L.tdb' on https://www.matca lc.at/[19] and archived in Mendeley Data.[20] The Open Data Commons Open Database License (ODbL v1.0) and Database Contents License (DbCL v1.0) apply.

REFERENCES

1. R.C. Reed, *The Superalloys* (Cambridge University Press, Cambridge, 2006).
2. A.K. Jena, and M.C. Chaturvedi, *J. Mater. Sci.* 19, 3121 (1984).
3. L. M. Pike, in *Superalloys 2008* (2008), pp. 191–200.
4. NiDI and INCO Ltd, *High-Temperature High-Strength Nickel Base Alloys* (1995).
5. W. P. Hughes, T. F. Berry, and R. E. Yount, *A Study of the Strain-Age Crack Sensitivity of Rene'41* (1968).
6. M. J. Donachie Jr and S. J. Donachie, *Superalloys: A Technical Guide*, 2nd ed. (2002).
7. C. T. Sims, N. Stoloff, and W. Hagel, in *Superalloys II* (Wiley, 1987), p. 615.
8. L.A. Weisenberg, and R. Morris, *Met. Prog.* 78, 70 (1960).
9. A.A. Luo, *Calphad Comput. Coupling Phase Diagrams Thermochem.* 50, 6 (2015).
10. M. Montakhab and E. Balikci, Metall. Mater. Trans. A Phys. Metall. Mater. Sci. **50**, 3330 (2019).
11. E. Kozeschnik, *Modeling Solid-State Precipitation* (Momentum Press, 2013).
12. M.G. Fahrmann, and D.A. Metzler, *Jom* 68, 2786 (2016).
13. R. Buerstmayr, F. Theska, R. Webster, M. Lison-Pick, and S. Primig, *Mater Charact* 178, 111250 (2021).
14. P. Villars, *Ni3Mo3C (Mo3Ni3C) Crystal Structure - PAULING FILE*, Multinaries. (Springer, Heidelberg, 2012).
15. P. Villars, *Cr23C6 Crystal Structure* (2016).
16. E. Povoden-Karadeniz, *Mc_fe_v2.060.Tdb* (Vienna, 2016).
17. H.E. Collins, and R.J. Quigg, *Trans. ASM* 61, 139 (1968).
18. H. E. Collins, Superalloys 171 (1968).
19. MatCalc, "mc_ni_L.Tdb," https://www.matcalc.at/index.php /databases/open-databases, 2023.
20. R. Buerstmayr, B. Schulz, E. Povoden-Karadeniz, E. Kozeschnik, M. Lison-Pick, and S. Primig, "mc_ni_L.Tdb", Mendeley Data, https://doi.org/10.17632/mnwnpfdw4n.1, 2023.
21. K. Song, and M. Aindow, *Mater. Sci. Eng. A* 479, 365 (2008).
22. J. Schindelin, I. Arganda-Carreras, E. Frise, V. Kaynig, M. Longair, T. Pietzsch, S. Preibisch, C. Rueden, S. Saalfeld, B. Schmid, J.-Y. Tinevez, D.J. White, V. Hartenstein, K. Eliceiri, P. Tomancak, and A. Cardona, *Nat. Methods* 9, 676 (2012).
23. I. Arganda-Carreras, V. Kaynig, C. Rueden, K.W. Eliceiri, J. Schindelin, A. Cardona, and H.S. Seung, *Bioinformatics* 33, 2424 (2017).
24. R. Buerstmayr, F. Theska, E. Kozeschnik, R.F. Webster, M. Lison-Pick, S.R. Street, and S. Primig, *Metall. Mater. Trans. A* 54, 2259 (2023).
25. G. Wang, L. Huang, X. Zhan, L. Tan, Z. Qin, W. He, and F. Liu, *Mater Charact* 178, 111178 (2021).
26. P. Warczok, *TechPaper #2014001: Evaluation of Interfacial Energies* (2014).
27. J. Svoboda, F.D. Fischer, P. Fratzl, and E. Kozeschnik, *Mater. Sci. Eng. A* 385, 166 (2004).
28. J. Stefan, *Proc. Imp. Philos. Acad. Math. Sci. Cl.* 79, 391 (1879).
29. G. Gottstein, *Physical Foundations of Materials Science* (Springer, Berlin, 2004).
30. U. Dehlinger, *Angew. Chemie* 48, 518 (1935).
31. P. Virtanen, R. Gommers, T. E. Oliphant, M. Haberland, T. Reddy, D. Cournapeau, E. Burovski, P. Peterson, W. Weckesser, J. Bright, S. J. van der Walt, M. Brett, J. Wilson, K. J. Millman, N. Mayorov, A. R. J. Nelson, E. Jones, R. Kern, E. Larson, C. J. Carey, İ. Polat, Y. Feng, E. W. Moore, J. VanderPlas, D. Laxalde, J. Perktold, R. Cimrman, I. Henriksen, E. A. Quintero, C. R. Harris, A. M. Archibald, A. H. Ribeiro, F. Pedregosa, P. van Mulbregt, A. Vijaykumar, A. Pietro Bardelli, A. Rothberg, A. Hilboll, A. Kloeckner, A. Scopatz, A. Lee, A. Rokem, C. N. Woods, C. Fulton, C. Masson, C. Häggström, C. Fitzgerald, D. A. Nicholson, D. R. Hagen, D. V. Pasechnik, E. Olivetti, E. Martin, E. Wieser, F. Silva, F. Lenders, F. Wilhelm, G. Young, G. A. Price, G.-L. Ingold, G. E. Allen, G. R. Lee, H. Audren, I. Probst, J. P. Dietrich, J. Silterra, J. T. Webber, J. Slavič, J. Nothman, J. Buchner, J. Kulick, J. L. Schönberger, J. V. de Miranda Cardoso, J. Reimer, J. Harrington, J. L. C. Rodríguez, J. Nunez-Iglesias, J. Kuczynski, K. Tritz, M. Thoma, M. Newville, M. Kümmerer, M. Bolingbroke, M. Tartre, M. Pak, N. J. Smith, N. Nowaczyk, N. Shebanov, O. Pavlyk, P. A. Brodtkorb, P. Lee, R. T. McGibbon, R. Feldbauer, S. Lewis, S. Tygier, S. Sievert, S. Vigna, S. Peterson, S. More, T. Pudlik, T. Oshima, T. J. Pingel, T. P. Robitaille, T. Spura, T.

R. Jones, T. Cera, T. Leslie, T. Zito, T. Krauss, U. Upadhyay, Y. O. Halchenko, and Y. Vázquez-Baeza, Nat. Methods **17**, 261 (2020).

32. J.D. Hunter, *Comput. Sci. Eng.* 9, 90 (2007).
33. M. G. Fahrmann and L. M. Pike, in *Miner. Met. Mater. Ser.* (Springer International Publishing, 2018), pp. 565–578.
34. A.S. Ebner, S. Jakob, H. Clemens, R. Pippan, V. Maier-Kiener, S. He, W. Ecker, D. Scheiber, and V.I. Razumovskiy, *Acta Mater.* 221, 117354 (2021).
35. F. Theska, R. Buerstmayr, H. Liu, M. Lison-Pick, S.R. Street, and S. Primig, *Mater Charact* 187, 111881 (2022).
36. M. Dodaran, A. H. Ettefagh, S. M. Guo, M. M. Khonsari, W. J. Meng, N. Shamsaei, and S. Shao, Intermetallics **117**, (2020).

37. M.P. Jackson, and R.C. Reed, *Mater. Sci. Eng. A* 259, 85 (1999).
38. E. Povoden-Karadeniz and A. Jacob, in *ESSC DUPLEX 2019 - 10th Eur. Stainl. Steel Conf. - Sci. Mark. 6th Eur. Duplex Stainl. Steel Conf. Exhib.* (2019), pp. 255–264.
39. C. Qiu, *J. Alloys Compd.* 199, 53 (1993).
40. T.Y. Velikanova, A.A. Bondar, and A.V. Grytsiv, *J. Phase Equilibria* 20, 125 (1999).